IV International Conference on Particle-based Methods – Fundamentals and Applications
PARTICLES 2015
E. Oñate, M. Bischoff, D.R.J. Owen, P. Wriggers & T. Zohdi (Eds)

DISCRETE ELEMENT SIMULATION OF WET GRANULAR MATERIALS: PLASTIC COMPRESSION

V.-D. THAN[1,2], J.-N. ROUX[1], A.-M. TANG[1] AND J.-M. PEREIRA[1]

[1] Université Paris-Est, Laboratoire Navier (UMR 8205), CNRS, ENPC, IFSTTAR,
F77455 Marne-la-Vallée Cedex 2, France
email: vinh-du.than@cermes.enpc.fr

[2] The University of Danang, College of Technology, Department of Civil Engineering,
48 Cao-Thang St., Hai-Chau Dist., Da Nang, Vietnam

Key words: Plastic compression, Capillary force, Consolidation, DEM

Abstract. We use Discrete Element Method (DEM) simulations in three dimensions (3D) to study the quasistatic response of very loose assemblies of frictional spherical grains to an isotropic compression in the presence of a small amount of an interstitial liquid, which gives rise to capillary menisci and attractive forces. Previous results obtained in 2D [8] are generalized to systems that may be observed in the laboratory. We study the influence of the initial assembling process and of various micromechanical parameters on the plastic compression curves, from very loose states assembled at low P^* to maximally compressed ones in which capillary cohesion is negligible at large P^*. We also show how the plastic response along those compression curves is influenced by rolling resistance in contacts.

1 INTRODUCTION

Many natural and industrial processes involve granular materials, in which grains are bonded, due to a variety of physical effects near intergranular contacts: capillary bridges, solid precipitation, artificial solid bridges. The water menisci joining solid particles in wet granular soils play a key role in the overall behavior studied in geotechnical engineering. Capillary cohesion bestows to these materials specific mechanical features that do not exist with dry grains, such as the ability to form stable structures at very low density, and a strong sensitivity to stress intensity as well as to stress direction. Published studies of bonded granular materials investigate the mechanical properties of cohesive soils (clays and silts) [18, 16], wet beads [6], cohesive powders [7, 8], loessic soils [4, 10], cemented sands [17, 11, 12, 2], or wet sands [15, 3]. The contact networks are hardly accessible to experiments, and intergranular forces are also inaccessible to measurements. Generally, the behavior of materials under a growing external load (oedometric or isotropic tests) is characterized by a compression curve showing an irreversible density increase with pressure.

"Discrete element"simulations, as introduced 35 years ago by Cundall & Strack [5], have become a valuable and efficient tool to investigate the microscopic mechanisms and to classify mechanical properties of granular systems. Cohesive granular materials, especially in loose states, have less frequently been investigated by numerical simulation than cohesionless ones. Inspired by the two-dimensional model for cohesive powders of Gilabert *et al.* [7, 8], a 3D model is developed to investigate the mechanical behavior of a model bonded granular soils (glass beads with capillary bonds in the pendular state). Results are presented for simulations of isotropic compression cycles, both for the macroscopic behaviour (plastic compression curve) and for the evolution of microstructural and micromechanical parameters.

2 MODEL MATERIAL

2.1 Intergranular forces

We consider assemblies of spherical beads of diameter a and mass m, with the elastic properties of glass: Young modulus $E = 70$ GPa, Poisson ratio $\nu = 0.3$. They interact in their contacts by the Hertz law, relating the elastic normal force F_N^E to the normal deflection h as

$$F_N^E = \frac{E}{3(1-\nu^2)}\sqrt{a}h^{3/2}. \tag{1}$$

This corresponds to a force-dependent normal stiffness $K_N = \frac{dF_N^H}{dh} = \frac{E}{2(1-\nu^2)}\sqrt{a}h^{1/2}$. The tangential force model, combining elasticity and friction, is described by [1]. Tangential stiffness K_T (relating increments of tangential elastic force and of tangential elastic displacement is proportional to K_N, $K_T = \dfrac{2-2\nu}{2-\nu}K_N$. Alternatively, a linear contact elasticity might be implemented, with h-independent stiffness coefficients K_N, K_T. The Coulomb condition $||\mathbf{F}_T|| \leq \mu F_N^E$, involving the sole repulsive elastic part of the normal force (Fig. 1(b)), is enforced with friction coefficient $\mu = 0.3$.

The attractive capillary force is only present if grains have been in contact and the meniscus has not broken since. A meniscus of volume V_m remains until separation distance reaches its rupture value, $D_r \simeq V_m^{1/3}$ [9]. We use the Maugis approximation [14] for capillary forces:

$$F_N^{cap} = -F_0\left[1 - \frac{1}{\sqrt{1+\frac{4V_m}{\pi a D^2}}}\right]. \tag{2}$$

D denotes here the distance between the surfaces of the particles joined by the liquid meniscus. $F_0 = \pi a\gamma\cos\theta$ is the maximum tensile force, involving surface tension γ of the water-air interface (7.27×10^{-2} N/m at 20^oC), and θ is the wetting angle, with $\theta = 0$ for a perfectly wetting liquid. Most calculations here are carried out with $V_m/(a^3) = 10^{-3}$, and thus the force range extends to $D_r = a/10$ (corresponding to a very small capillary force). This ratio of meniscus volume V_m to a^3 is one of the dimensionless

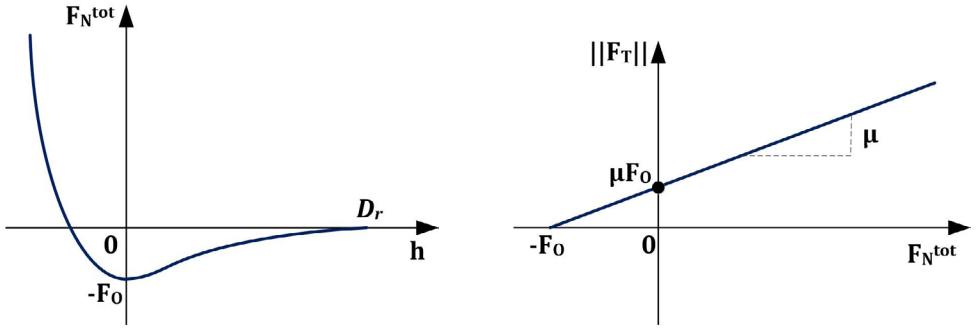

(a) (b)

Figure 1: (a) Static normal force, $F_N = F_N^E + F^{cap}$, versus deflection h or distance $D = -h$. (b) Coulomb cone limiting the value of the tangential force.

control parameters in the present study, determining the number of liquid bonds and the range of the corresponding capillary attraction. Our work is limited to the pendular state of isolated menisci [15].

The total static normal force combines the elastic normal force (Hertzian force) and the capillary force, $F_N^{tot} = F_N^E + F_N^{cap}$, as shown in Fig. 1(a). A viscous force is added in contacts, opposing the normal relative velocity of grains as in [1], in order to damp the vibrations about equilibrium states – with no notable influence on quasistatic rheology.

Two particles moving away from each other after a collision will only separate if their receding relative velocity is large enough to overcome the capillary force, i.e. larger than a threshold proportional to V^* [7], with

$$V^* = \sqrt{\frac{F_0 D_r}{m}}. \tag{3}$$

The influence of *rolling resistance* (RR) at contacts, as investigated in 2D in [8], is also studied. For simplicity, we only implement this feature with linear contact elasticity. The existence of RR is related to the particle surface roughness, such that contact regions are larger than the ones deduced from contact elasticity. Four additional parameters are necessary: (i) a *rolling spring constant* K_R which expresses the proportion between relative rotation and rolling moment (in the tangential plane), as long as the rolling friction threshold is not reached; (ii) a *pivoting spring constant* K_P (chosen equal to K_R), relating similarly the pivoting moment to the pivoting (i.e., along the normal direction) relative rotation angle; (iii) a *rolling friction coefficient* μ_R with the dimension of a length, setting the maximum norm of the rolling moment $||\Gamma_R||$ to $\mu_R F_N^E$, proportional to the elastic part of the normal force; and (iv) a *pivoting friction coefficient* μ_P (chosen equal to μ_R), requesting similarly the absolute value of the pivoting moment to stay below $\mu_P F_N^E$. In most simulations with RR, we set μ_R/a=0.02, $K_R/(K_N a^2) = 2.5 \times 10^{-5}$ while $K_T/K_N = 1$ and $K_N/a = 4$ GPa.

2.2 Stress control and equilibrium

Numerical samples comprise N=4000 equal-sized spherical beads of diameter a and mass m, with no gravity, within a cuboidal cell with periodic boundary conditions. The cell edges are parallel to the coordinate axes $(x_\alpha)_{\alpha=1,3}$. Their lengths $(L_\alpha)_{\alpha=1,3}$ vary simultaneously with the grain positions until a mechanical equilibrium state is achieved for all particles with externally imposed values $(\Sigma_\alpha)_{1\leq\alpha\leq3}$ of principal stresses:

$$\sigma_{\alpha\alpha} = \frac{1}{\Omega}\left[\sum_i m_i v_i^\alpha v_i^\alpha + \sum_{i<j} F_{ij}^{(\alpha)} r_{ij}^{(\alpha)}\right]. \tag{4}$$

Here, $\Omega = L_1L_2L_3$ is the sample volume, $r_{ij}^{(\alpha)}$ is coordinate α of vector $\mathbf{r}_{ij}$ joining the centers of neighbor beads i and j and $F_{ij}^{(\alpha)}$ the corresponding force coordinate. Velocities $\mathbf{v}_i$ of grain centers comprise, in addition to a periodic field, an affine term corresponding to the global strain rate. Equations of motion for dimensions L_α are written in addition to the ordinary equations for the dynamics of a collection of solid objects, and they drive the system towards an equilibrium state in which conditions $\sigma_{\alpha\alpha} = \Sigma_\alpha$ are satisfied [1]. A typical intergranular force value F_1=max(F_0, Pa^2) sets the tolerance levels for individual grain equilibrium, where P is the applied pressure. A configuration is deemed equilibrated when the following conditions are simultaneously satisfied: (i) the net force (the total force) on each spherical grain is less than $10^{-4}F_1$; (ii) the total moment on each sphere is lower than $10^{-4}F_1a$; (iii) the difference between imposed and measured stresses is less than $10^{-4}F_1/a$; and (iv) the kinetic energy per grain is less than $10^{-7}F_1a$.

2.3 Dimensionless control parameters

While calculations are carried out with glass beads of diameter $a = 0.11$ mm, assuming perfect wetting ($\theta = 0$), it is convenient to express dimensionless results as functions of dimensionless input parameters, thereby achieving greater generality. Aside from the friction coefficient, the important dimensionless combinations are the reduced pressure, $P^* = a^2P/F_0$, comparing the applied pressure to the tensile strength of contacts, and the stiffness parameter $\kappa = [E/P(1-\nu^2)]^{2/3}$ (for Hertzian contacts), or $\kappa = K_N/P$ (for linear elasticity). $P^* \ll 1$ in cohesion-dominated systems, for which attractive forces may stabilize loose structures. Confining forces dominate for $P^* \gg 1$, and attractive forces become negligible. For the chosen value of a, $P^* = 1$ corresponds to $P = 2$ kPa. κ, on the other hand, sets the typical scale of deflections h under confining forces, as $h/a \sim \kappa^{-1}$ [1]. The simulation parameters are chosen such that P^* reaches large values before κ^{-1} decreases to 10^{-3}. Additional parameters are $\mu_R/a = \mu_P/a$ in systems with RR, as well as the rotation angles for which rolling and pivoting friction thresholds are reached (small enough to be irrelevant in our case).

Table 1: Initial configurations

Φ_0	V_0/V^*	V_m/a^3
0.30	0.2041	1.00×10^{-3} (reference case)
0.30	0.4082	1.00×10^{-3}
	1.2247	
	4.0825	
	12.2474	
	40.8248	
0.30	0.2041	5.00×10^{-4} | 2.50×10^{-4}
		1.25×10^{-4} | 6.25×10^{-5}
		3.13×10^{-5} | 1.56×10^{-5}
		7.80×10^{-6}
0.32	0.2041	1.00×10^{-3}
0.35	0.2041	1.00×10^{-3}
0.40	0.2041	1.00×10^{-3}
0.45	0.2041	1.00×10^{-3}

3 NUMERICAL PROCEDURES

3.1 Specimen preparation

We first use a hard sphere event-driven method to prepare disordered, low density configurations of 4000 grains. All particles are then launched with Gaussian-distributed random velocities with quadratic mean V_0. They collide and stick to one another within a cell of constant size, forming larger and larger aggregates. Finally, all grains are connected to one another by cohesive contacts and reach an equilibrium position. This initial structure depends on one dimensionless parameter, characterizing the agitation intensity in the assembling stage. It is defined as the ratio of V_0 to the minimum receding velocity V^* introduced in Eq. (3). As in Ref. [7], larger initial agitation levels are observed to produce better connected structures. The initial parameters are listed in Table 1.

3.2 Compaction process

The final packing structures is compacted under growing external isotropic pressure. The main objective of the present paper is the study of the effect of a gradual compression, starting from cohesion-dominated loose states at small P^*, and ending in confinement-dominated denser states at large P^*. A stepwise pressure-controlled loading path is applied. In each compression step, pressure P^* is multiplied by a constant factor $10^{1/4} \simeq 1.7783$, and one waits until the new equilibrium configuration is reached, within the tolerance criteria stated in Sec.2.2. The compression program is pursued until P^*_{max}, well beyond complete plastic collapse is obtained. Then, the effect of P^* back to minimum value from its highest value is also simulated.

4 NUMERICAL RESULTS

4.1 Reference case

A typical test is run with a low initial solid fraction, $\Phi_0 = 0.30$. The results are shown in the from of the conventional compression curve $e - \log(P)$ in Fig. 2. Three regimes

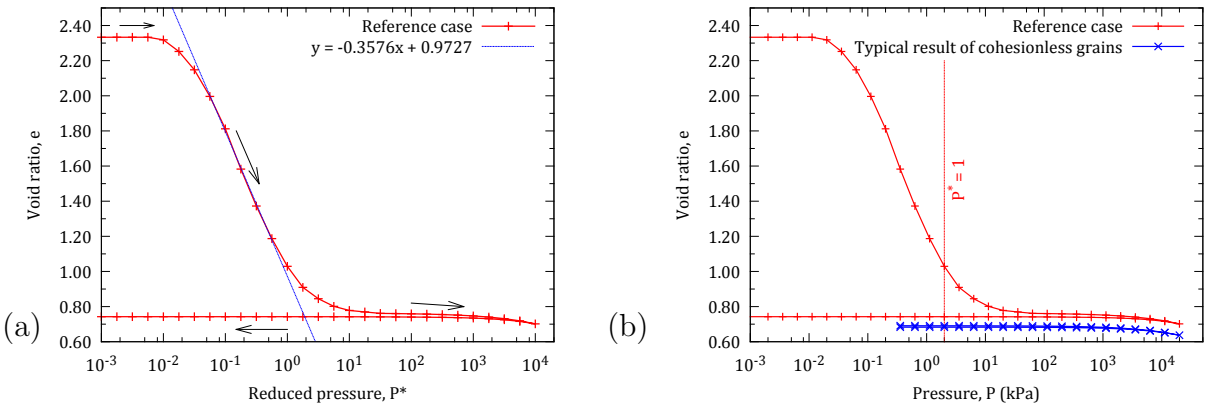

Figure 2: (a) Compression and decompression curves in reference case, with (b) comparison with cohesionless systems.

can be distinguished in the compression curve, for different pressure ranges. A first regime, thereafter called regime **I**, is observed for low reduced pressures P^*, in which the initial structure still sustains the increasing pressure without rearranging, and void ratio e remains nearly constant. In regime **II**, roughly corresponding to interval $0.02 \leq P^* \leq 2$, void ratio strongly decreases, and might be described as linearly varying with $\log P^*$. The loose structures formed at low P^* are no longer able to support the increasing confining pressure, they collapse and restructure. Finally, in regime **III**, e gradually approaches some minimum void ratio e_{min} at the end of the loading process. The slight decrease of e for $P^* \geq 100$ is similar to the cohesionless result, and due to elastic deflections in a stable contact network. The chosen parameters are such that κ remains large enough not to influence the compression process taking place in regime **II**. Upon decompression, e increases slightly, remaining very close to e_{min}: the compaction is essentially irreversible, unlike in the cohesionless granular assembly of Fig. 2(b), for which loading and unloading branches are not distinguishable. The compression curve is similar to the ones obtained by Gilabert *et al.* [8]. An important microstructural characteristic, the coordination number z, defined as the average number of interactions per grain, is the sum of the contact coordination number z_c and the coordination number of distant interactions, through menisci joining non-contacting grains, z_d. Fig.3 plots z_c, z_d, and z versus P^* in the compression cycle. Initially, one has $z_d = 0$, as the velocities in the aggregation process, in

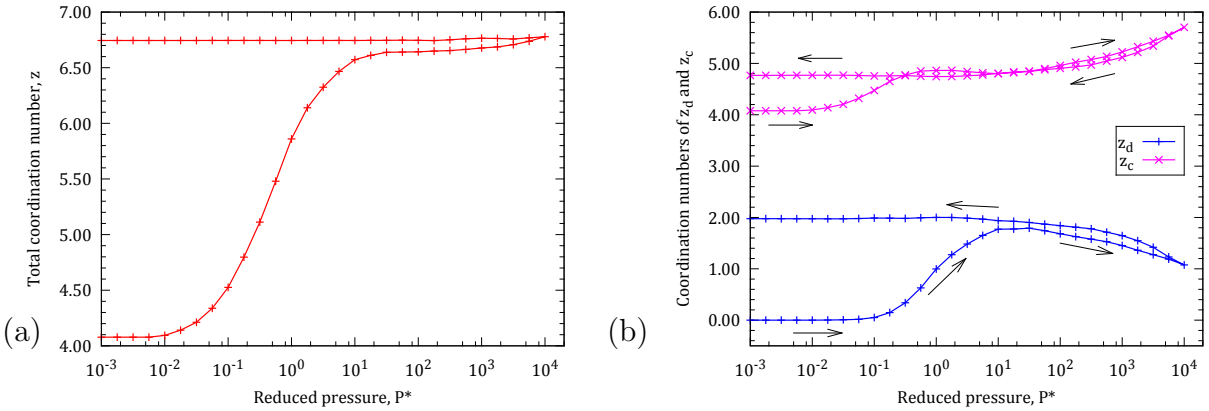

Figure 3: Coordination numbers in reference system subjected to the pressure cycle: z (a); and z_c and z_d (b), versus P^*.

the reference case, are low, and do not allow contact opening. z_c and z_d remain unchanged in regime **I**. Both coordination numbers start to increase as the structure collapses and reorganizes in regime **II**. z exhibits little change in regime **III**, showing that the increase of the number of contacts is mainly due to the closing of narrow gaps between pairs of grains joined by a meniscus, as the structure is further compressed – a moderate effect, partly reversed upon unloading. Further unloading back to small pressures takes place with nearly constant coordination numbers of both types, reflecting the stability of the dense structure formed at high P^*.

4.2 Effect of initial solid fraction

Among the features affected by the assembling process, the competition between compression and aggregation is the most important one. Fig. 4, obtained with standard values $V_0/V^* = 0.2041$, $V_m/a^3 = 10^{-3}$, compares the compression curves of specimens with different initial solid fractions Φ_0 (the red arrow denotes the increase of Φ_0). Denser systems are able to support larger pressures before rearranging, whence larger regime **I** plateaus (see Fig. 4(a)). However, in regime **II**, these compression curves start to converge and very nearly coincide in regime **III**. Coordination numbers z_c and z_d are and remain almost equal whatever the initial Φ_0 (see Fig. 4(b)).

4.3 Effect of initial agitation intensity

Ratio V_0/V^*, characterizing the intensity of initial agitation and its ability to break adhesive contacts, strongly influences the initial assembling process and the resulting coordination number. Fig. 5 shows that this parameter mainly affects the beginning of the compression curve. Six different values of V_0/V^* are used, the difference between

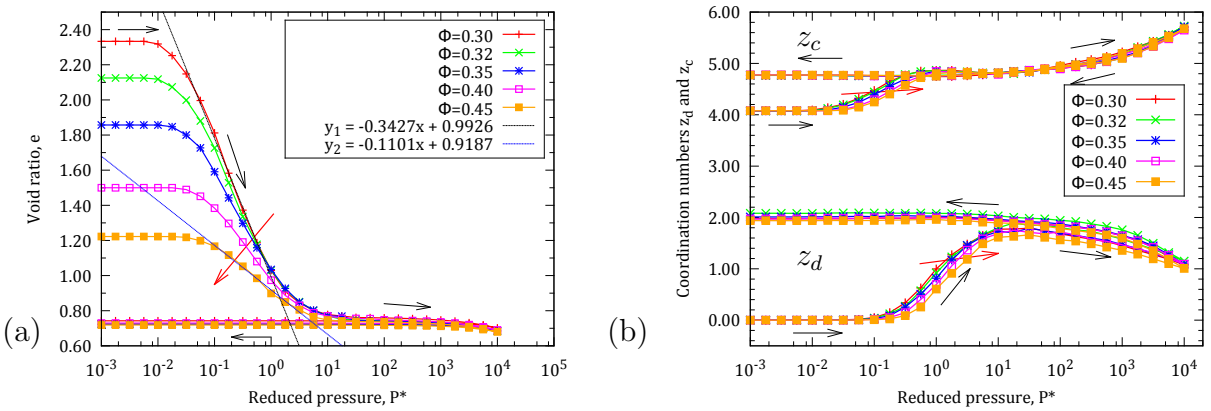

Figure 4: (a) Void ratio e and (b) coordination numbers z_c and z_d versus P^* in compression cycle for different values of Φ_0.

minimum and maximum values is two-hundredfold. Under low P^*, the wider regime **I** plateaus correspond to the higher initial agitation velocities. I If initial velocity V_0 is of the order of V^*, the initial packing structure is strongly perturbed. I n other words, the larger the velocity, the stronger the initial structure (see Figure 5(a)), with more contacts – relatively strong increases in initial coordination numbers z_c and z_d are observed at low P^* (see Figure 5(b)). Conversely, with low agitation velocities ($V_0 \leq V^*$), grains stick gently to one another and clusters of aggregated grains are not disturbed. In other words, lower agitation velocities induce more tenuous aggregates.

4.4 Effect of meniscus volume

We now report on investigations of the influence of meniscus volume V_m/a^3, which is kept low enough for the material (with a saturation hardly exceeding 1%) is maintained in the pendular state. Despite the importance of capillary bridges in the stabilization of loose structures, changing the meniscus volume (or liquid content) seems to have no effect on the macroscopic behaviour of the granular specimens under isotropic compression (no apparent change in the compression curve, e versus $\log P^*$). This is corroborated by the fact that very little change in the coordination number of contacts z_c is observed. Only the coordination number of distant interactions is notably influenced by such a change, especially in regimes **II** and **III**, and in the decompression process, as shown in Fig. 6. As menisci break at larger interparticle distance with larger meniscus volume, more liquid bonds are present.

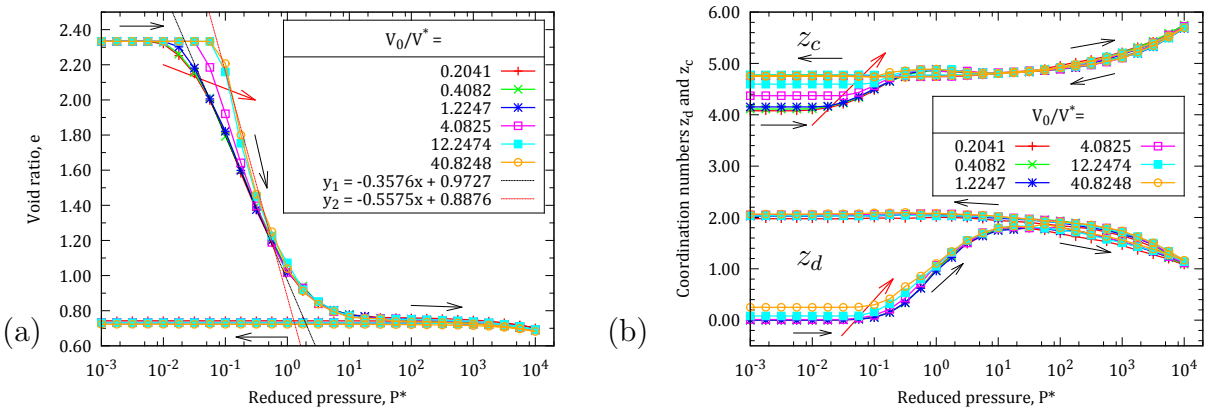

Figure 5: (a) Compression and decompression curves and (b) coordination numbers z_c and z_d for the reference case with different values of V_0/V^*.

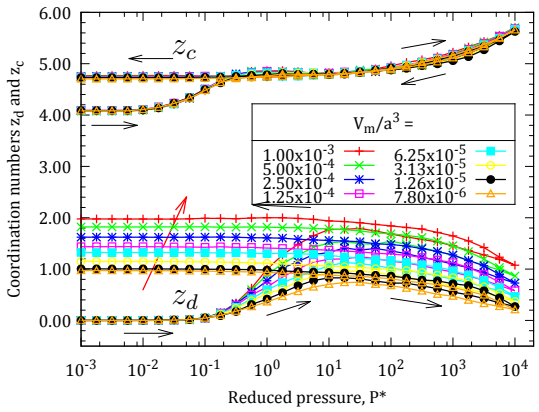

Figure 6: Coordination number z_c, z_d, $z = z_c + z_d$ for standard values $\Phi_0 = 0.30$, $V_0/V^* = 0.2041$ and for different values of V_m/a^3.

4.5 Effect of rolling resistance

Fig. 7 shows the effect of initial velocities V_0 and rolling/pivoting friction coefficients $\mu_R/a = \mu_P/a = 0.02$ on the initial assembling process and coordination numbers for Φ_0=0.30 and $V_m/a^3 = 10^{-3}$. For the smallest velocities, the appearance of RR in contacts creates denser systems under low P^*, with smaller coordination numbers. Unlike the initial loose structures formed without RR, which can sustain a small non-vanishing pressure in regime **I**, the compression curve of the tenuously connected (with coordination number approaching 2, i.e., virtually no loop) initially formed with RR, and a low

agitation velocity, responds by some plastic collapse at the first pressure increment, as shown in Fig. 7(a). Its regime **I**, if it exists, is confined to much smaller pressures. It reappears on the pressure scale of Fig. 7(a) in systems assembled with larger initial agitation velocities, which are better coordinated (Fig. 7(b)), and collapse more abruptly in plastic compression. Interestingly, the system assembled with the lower coordination numbers first react by plastic compression without contact loss, as z_c is constant and z_d remains equal to zero (no contact opening creating a distant interaction). More complete

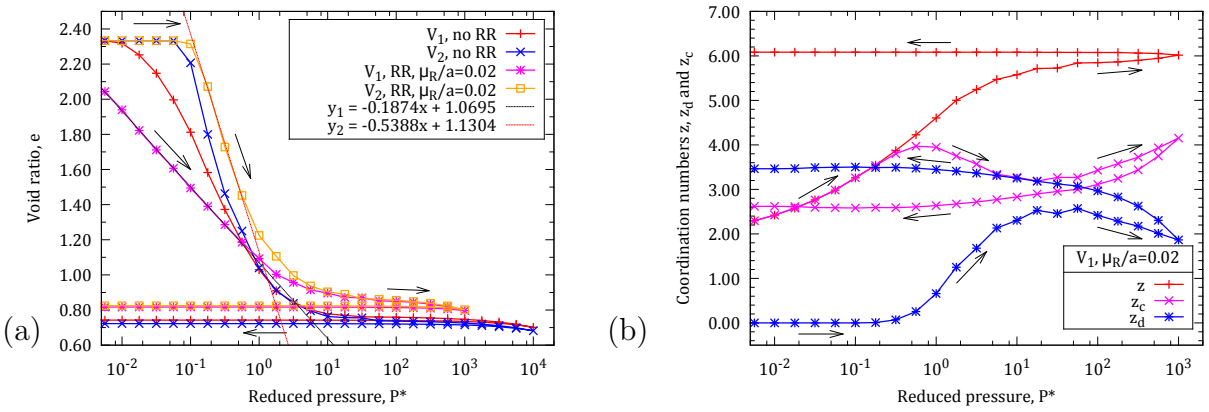

Figure 7: Void ratio e (a) and coordination numbers z_c, z_d and $z = z_c + z_d$ (b) versus P^* in pressure cycle for different systems with or without RR ($V_1 = V_0/V^* = 0.2041$, $V_2 = V_0/V^* = 40.8248$).

analyses of the corresponding structural changes are being carried out, and their results will be published in forthcoming papers.

5 CONCLUSIONS AND OUTLOOK

Our results show that the simple model of wet granular materials implemented in our simulations exhibit the familiar plastic compression properties of cohesive soils or powders, with a well defined limit of gently assembled (minimally coordinated) structures, and low initial densities, such that the behaviour does not depend on dynamical model ingredients. A small level of rolling and pivoting friction is enough to produce strong differences in the plastic behaviour, with the collapse under growing confining pressure becoming notably more gradual.

The research program developed here can be extended in several directions. For example, the quasistatic behavior of a 3D model accounting for the effect of rolling resistance under oedometer and triaxial tests, in pendular state, is a straightforward extension of the present work. The role played by solid bridges instead of capillary bonds could also be investigated.

ACKNOWLEDGMENTS

The first author of the paper is supported by the Scholarship (the Project No 911) of Ministry of Education and Training, the Vietnamese Government to do this work.

REFERENCES

[1] Agnolin, I. and Roux, J.-N. Internal states of model isotropic granular packings. i. assembling process, geometry, and contact networks. *Phys. Rev. E* (2007) **76**:061302

[2] de Bono, J., McDowell, G. and Wanatowski, D. Investigating the micro mechanics of cemented sand using DEM. *International Journal for Numerical and Analytical Methods in Geomechanics* (2014) **10**:n/a-n/a

[3] Bruchon, J.-F., Pereira, J.-M., Vandamme, M., Lenoir, N., Delage, P., Bornert, M. Full 3d investigation and characterization of capillary collapse of a loose unsaturated sand using X-ray CT. *Granular Matter* (2013) **15**:783-800

[4] Muñoz Castelblanco, J., Delage, P., Pereira, J.-M and Cui, Y.J. Some aspects of the compression and collapse behavior of an unsaturated natural loess. *Géotechnique Letters* (2011) **1**: 17-22

[5] Cundall, P. and Strack, O. A discrete numerical model for granular assemblies. *Géotechnique* (1979) **29**: 47-65

[6] Fournier, Z., Geromichalos, D., Herminghaus, S., Kohonen, M., Mugele, M., Scheel, F., Schulz, M., Schulz, B., Schier, C., Seemann, R. and Skudelny, A. Mechanical properties of wet granular materials. *J. Phys.: Condens. Matter* (2005) **17**:S477

[7] Gilabert, F., Roux, J.-N., Castellanos, A. Computer simulation of model cohesive powders: Influence of assembling procedure and contact laws on low consolidation states. *Phys. Rev. E* (2007) **75**: 011303

[8] Gilabert, F., Roux, J.-N., Castellanos, A. Computer simulation of model cohesive powders: Plastic compression, structural changes, and elasticity under isotropic states. *Phys. Rev. E* (2008) **78**: 031305

[9] Herminghaus, S. Dynamics of wet granular matter. *Advances in Physics* (2005) **54**: 221-261

[10] Jiang, M., Hu, H. and Liu, F. Summary of collapsible behavior of artificially structured loess in oedometer and triaxial wetting tests. *Canadian Geotechnical Journal* (2012) **49**: 1147-1157

[11] Jiang, M., Yan, H., Zhu, H. and Utili, S. Modeling shear behavior and strain localization in cemented sands by 2D distinct element method analyses. *Computer and Geotechnics* (2011) **38**: 14-29

[12] Jiang, M., Zhang, W., Sun, Y. and Utili, S. An investigation on loose cemented granular materials via DEM analyses. *Granular Matter* (2013) **15**: 65-84

[13] Johnson, K. L. *Contact Mechanics*. Cambridge University Press (1985)

[14] Maugis, D. *Contact, Adhesion and Rupture of Elastic Solids*. Springer Berlin Heidelberg, Springer Series in Solid-State Sciences 130, (2000).

[15] Mitarai, N. and Nori, F. Wet granular materials. *Advances in Physics* (2006) **55**: 1-45.

[16] Mitchell, J. and Soga, K. *Fundamentals of Soil Behaviour*. Wiley, New York (2005).

[17] Wang, Y and Leung, S. Characterization of cemented sand by experimental and numerical investigations. *Journal of Geotechnical and Geoenvironmental Engineering* (2008) **134**: 992-1004.

[18] Wood, D. M. *Soil Behaviour and Critical State Soil Mechanics*. Cambridge University Press, (1990).